An Automatic Spatial-Temporal Evolution Inversion Method of Mining Goaf Based on the Improved Hotspot Analysis and Probability Integral Method

Lu Li, Jili Wang, *Member, IEEE*, Heng Zhang, *Member, IEEE*, Yi Zhang, Yingjie Wang, and Yuanzhao Fu

***Abstract*—Mining activities may cause severe ground subsidence, endangering surface structures, and farmlands. Therefore, the acquisition of spatial-temporal evolution of the mining goaf is of great significance. Hotspot analysis (HSA) based on the Getis-Ord G_i^* statistics has been utilized to identify the areas with a rapid deformation rate. In this article, we propose an improved HSA (IHSA) method for automatic extraction of the surface subsidence caused by the mining goaf. In addition, we design a comprehensive workflow for the automatic spatial-temporal evolution inversion of surface deformation induced by the mining goaf. First, time series interferometric synthetic aperture radar (InSAR) is utilized to generate the surface deformation of the mining area. Then, the IHSA method is used for the automatic identification of the mining goaf. Finally, the total least-squares probability integral method (TLS-PIM) is applied for goaf inversion based on the extracted deformation information. For this study, the Wuxiang is selected as the study area. We have compared the IHSA method with four methods using five indicators, and likewise, we have compared the TLS-PIM method with four methods in terms of their correlation with the InSAR results in the strike and dip directions. The experimental results demonstrate the superiority of our method as a support for the geological hazard investigation and mine safety supervision department.**

***Index Terms*—Goaf identification, hotspot analysis (HSA), probability integral method (PIM), time series interferometric synthetic aperture radar (TS-InSAR).**

I. Introduction

MINING activities disrupt the natural stress balance of surrounding rock formations [1] and lead to geological hazards, such as collapse pits and subsidence basins, which pose a severe threat to structures and farmland. It remains challenging to monitor the safety of the mining area [2]. First, unauthorized or illegal mining activities are often concealed and difficult to detect. Second, mines are typically located in rugged terrain. Lastly, optical images have inherent limitations related to weather conditions. Conventional monitoring approaches, such as field surveys, leveling surveys, and Global Navigation Satellite System (GNSS), are often time-consuming and labor-intensive [3]. To overcome these challenges, it is essential to develop more efficient, cost-effective alternative monitoring methods with extensive spatial coverage. In recent years, interferometric synthetic aperture radar (InSAR) has been utilized to generate surface deformation and offers extensive spatial coverage with high measurement accuracy. Surface deformation is a critical indicator for the identification of potential geological hazards, including mining goafs [4]. Furthermore, time series InSAR (TS-InSAR) mitigates the influence of spatial-temporal decorrelation, atmospheric delay, and satellite orbit error, generating precise deformation [5]. Researchers have integrated InSAR with other auxiliary information, such as GNSS [6] and leveling data [7], to enhance the robustness of the method. During underground coal mining, geological hazards may occur as the overlying strata above the mining goaf sinks [8]. Hence, for monitoring the safety of the mining area, it is essential to understand the spatial-temporal evolution characteristics of the mining goaf The above analysis involves two components: identification and inversion. For the former, visual interpretation and invariant threshold segmentation methods are frequently used for the identification of geological hazards [9], [10]. However, these methods present challenges in generalization due to the numerous mining sites and complex geological environments. The coherence-based identification approach [11], [12] is limited by image acquisition interval and the inability to identify small-scale mining goafs. Spatial clustering methods, such as hotspot analysis (HSA), effectively identify areas of anomalous deformation. Lu et al. [13] calculated the steepest descent direction from the digital elevation model (DEM) to determine the search distance and applied HSA for landslide detection. Lu et al. [14] determined the distance through incremental spatial autocorrelation, a novel idea that, however, bears a computationally intensive process. Zhu et al. [15] addressed geometric distortion influence through visibility analysis and employed the HSA method for landslide detection, though they did not consider outliers, which affected the method's effectiveness.

Manuscript received 15 August 2023; revised 16 October 2023; accepted 5 November 2023. Date of publication 17 November 2023; date of current version 14 December 2023. This work was supported by the National Natural Science Foundation of China under Grant 62001451, and in part by Civil Space Thirteen Five Years Pre-Research Project under Grant D040114. *(Corresponding author: Jili Wang.)*

Lu Li and Yuanzhao Fu are with the Department of Space Microwave Remote Sensing System, Aerospace Information Research Institute, Chinese Academy of Sciences, Beijing 100190, China, and also with the School of Electronic, Electrical and Communication Engineering, University of Chinese Academy of Sciences, Beijing 101408, China (e-mail: lilu21@mails.ucas.edu.cn; fuyuanzhao21@mails.ucas.ac.cn).

Jili Wang, Heng Zhang, Yi Zhang, and Yingjie Wang are with the Department of Space Microwave Remote Sensing System, Aerospace Information Research Institute, Chinese Academy of Sciences, Beijing 100190, China (e-mail: wangjl01@aircas.ac.cn; zhangheng@aircas.ac.cn; zhangyi@aircas.ac.cn; wangyingjie113@mails.ucas.ac.cn).

Digital Object Identifier 10.1109/JSTARS.2023.3333963

Dai et al. [16] chose the minimum distance as the search distance. However, due to insufficient distance, identified hotspots tend to cluster, rendering the results less reliable. Selecting an optimal distance is the key to the identification of deformation areas for the HSA [17]. Hence, the determination of optimal parameters and the removal of outliers are worth further research for the identification of the mining goaf.

InSAR measures the surface deformation along the line of sight (LOS), which restricts the understanding of the movement mechanisms of the mining goaf [18]. Efforts [19], [20] have been made to overcome this limitation, particularly the integration with relevant data, such as offset tracking data [21], [22], airborne data [23], [24], leveling data [25], GPS data [26], and other auxiliary data [27], [28]. Another widely used strategy is the probability integral method (PIM) [29], [30], which is based on the surface movement model, and is frequently combined with TS-InSAR for subsidence analysis in mining areas. The subsidence information of the identified mining goaf contributes to determining optimal parameters required by the model and enhances the comprehension of the spatial-temporal evolution of the mining goaf.

Based on existing problems and previous studies, we propose an improved HSA (IHSA) method for the study of spatial-temporal evolution inversion of the mining goaf. The method combines the HSA method with recursive incremental spatial autocorrelation (HSA-RISA) and *k*th average nearest neighbor density-based spatial clustering of applications with noise (KANN-DBSCAN) method. The key steps of this method comprise the following.

1) TS-InSAR is utilized to generate surface deformation in the mining area.
2) Feature scatterers are extracted based on the HSA-RISA method.
3) The KANN-DBSCAN method is employed to identify the mining goaf.
4) The total least-squares the probability integral method (TLS-PIM) is applied for goaf inversion based on the extracted deformation information of the mining goaf from the IHSA method.

The method is applied in Wuxiang, where 24 goafs have been identified, including eight endangering villages (see Fig. 13).

The rest of this article is organized as follows. Section II describes the study area, datasets, and the methodology of key steps in our proposed workflow. Section III presents the experimental results and analysis of spatial-temporal evolution characteristics. Section IV discusses the experimental results. Finally, Section V concludes this article.

II. Methodology, Study Area, and Datasets

A. Methodology

Fig. 1. presents the flowchart of the proposed method, which is partitioned into four parts.

1) TS-InSAR Method: A standard TS-InSAR procedure is applied to all SAR images. The coregistration of other images is achieved using auxiliary data (e.g., precise orbit data and DEM data) and the super master image. Multilooking processing [31] is employed to ensure that images have similar spatial resolution in range and azimuth directions while also mitigating the effect of speckle noise. The baseline error present in the interferogram is removed based on a quadratic polynomial model [32]. Correction for atmospheric phase is accomplished using a spatially variable power-law tropospheric correction method [33]. Singular value decomposition (SVD) is applied to obtain the minimum parametric solution for the velocity vector and the linear deformation information [34]. The atmospheric and nonlinear deformation phases obtained through SVD are then filtered in the spatial and time domains, respectively. Finally, two deformation maps are generated, including the annual deformation velocity map and the time-series cumulative deformation map.

2) Feature Scatterers Extraction Based on the HSA-RISA Method: HSA is used to quantify the spatial dependence, aiding in the identification of potential mining goafs [35]. However, the search distance influences hotspot identification [15]. Determining search distance from DEMs affects algorithm efficiency [13]. An effective way to determine the optimal spatial distance is by considering the statistical properties of the dataset, which can be calculated through the spatial autocorrelation at different distances, referred to as incremental spatial autocorrelation. The corresponding distance at which Moran's Index reaches its maximum, as calculated by the above method, is the optimal spatial distance. Besides, the Getis-Ord G_i^* statistic reflects the statistical significance of spatial clustering [14]. The Z-score, obtained by analyzing the standard deviation, and the P-value derived from evaluating the independent probability, are employed to assess the statistical significance of spatial clustering for all measurement scatterers (MSs) [15].

Specifically, the time complexity of computing the Moran's Index is $\mathbf{O}(\mathrm{n}^2)$, where n is the number of MSs. When n is large, the required time becomes significant. To address this, a recursive idea is introduced to determine the optimal search distance. Assuming an initial spatial distance interval $[R_1, R_n]$, where d_1 is the initial distance step, the algorithm is implemented as follows.

$$I_{R_1+k_1d_1} = \begin{cases} \frac{n_0}{S_{R_1+k_1d_1}} \frac{\sum_{i=1}^{n}\sum_{j=1}^{n} w_{(ij,R_1+k_1d_1)}(v_i-\bar{v})(v_j-\bar{v})}{\sum_{j=1}^{n}(v_j-\bar{v})^2} & if\ \mathrm{Euc}(v_j,v_i) \le R_1+k_1d_1 \\ 0 & if\ \mathrm{Euc}(v_j,v_i) > R_1+k_1d_1 \end{cases}$$
$$k_1 = (0,1,2,\ldots,n_1)$$
$$R_1 \le R_1 + k_1d_1 \le R_n. \tag{1}$$

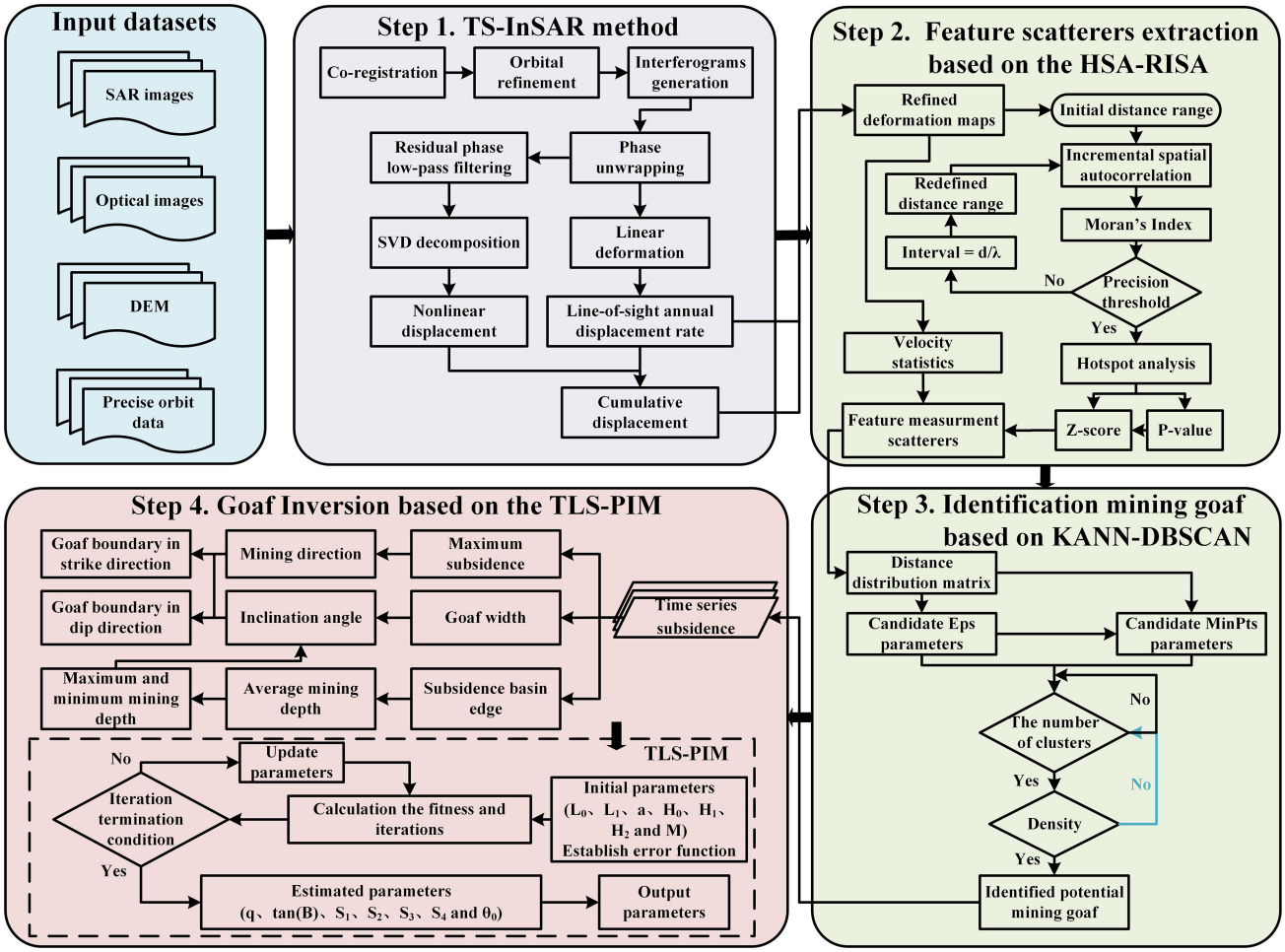

Fig. 1. Flowchart of the proposed method.

Step 1: An iterative average nearest neighbor and median nearest neighbor [36] can be utilized to remove outliers that affect the calculation of statistical indicators. This leverages the law of large numbers by applying a three-sigma criterion to the nearest neighbor of MSs.

Step 2: The spatial autocorrelation of the scene is estimated using the Moran's Index, computed by (1) shown at the bottom of the previous page, where n_0 is the total number of MSs. $\bar{v}$ is the mean velocity of MSs, $\mathrm{Euc}(v_j, v_i)$ is the Euclidean distance between v_j and v_i, $S_{R_1+k_1d_1}$ is the sum of spatial weight when the search distance is $R_1 + k_1d_1$. The spatial weight $w_{(ij,R_1+k_1d_1)}$ can be expressed as

$$w_{(ij,R_1+k_1d_1)} = \begin{cases} \frac{1}{|(v_j - v_i)^\gamma|} & if\,\mathrm{Euc}(v_j, v_i) \le R_1 + k_1d_1 \\ 0 & if\,\mathrm{Euc}(v_j, v_i) > R_1 + k_1d_1 \end{cases} \quad (2)$$

where γ is the weight.

$$\begin{aligned} I_1^{\max} &= \max\{I_{R_1+k_1d_1}\} \\ k_1 &= (0, 1, 2, \ldots, n_1) \\ R_1 \le R_1 + k_1d_1 &\le R_n \end{aligned} \quad (3)$$

where $I_1^{\max}$ is the maximum of the initial interval and $I_{R_1+k_1d_1}$ corresponds to the local optimal distance D_1 in $[R_1, R_n]$.

Step 3: The distance interval is $[D_1 - d_1, D_1 + d_1]$. The distance step is reduced to $d_2 = d_1/\eta$. η is the interval scale factor. The maximum of the correlation surface is calculated using (4)

$$\begin{aligned} I_2^{\max} &= \max\{I_{D_1-d_1+k_2d_2}\} \\ k_2 &= (0, 1, 2, \ldots, n_2) \\ D_1 - d_1 \le D_1 - d_1 + k_2d_2 &\le D_1 + d_1 \end{aligned} \quad (4)$$

where $I_2^{\max}$ corresponds to the local optimal distance D_2.

Step 4: The spatial distance interval is $[D_2 - d_2, D_2 + d_2]$. The distance step is reduced to $d_3 = d_2/\eta$, and the maximum of the correlation surface is calculated using (5)

$$\begin{aligned} I_3^{\max} &= \max\{I_{D_2-d_2+k_3d_3}\} \\ k_3 &= (0, 1, 2, \ldots, n_3) \\ D_2 - d_2 \le D_2 - d_2 + k_3d_3 &\le D_2 + d_2 \end{aligned} \quad (5)$$

where $I_3^{\max}$ corresponds to the local optimal distance D_3. If the accuracy of $|d_3|$ reaches the threshold, D_3 represents the optimal search distance. Otherwise, return to step 3.

Step 5: The Getis-Ord G_i^* statistics are employed to calculate the spatial variability of each MS

$$G_i^*(d) = \frac{\sum v_{i,d} + v_i - n_{i,d} \times \bar{v}_{all}}{\sqrt{S_{all}\left\{[(n_{all} \times n_{i,d}) - {n_{i,d}}^2]/(n_{all} - 1)\right\}}} \quad (6)$$

where i represents the reference MS, d represents the search distance, n_{all} represents the number of all MSs, $n_{i,d}$ represents the number of MSs within the distance d from the reference MS, v_i represents the deformation rate of the reference MS, $v_{i,d}$ represents the deformation rate of MSs within the distance d from the reference MSs. $\bar{v}_{\text{all}}$ represents the deformation rate average of all MSs, and S_{all} represents the standard deviation of deformation rate of all MSs.

Step 6: A threshold of ± 1.96 for the Z-score and a threshold of 95% for the P-value are set to identify the hotspots within the study area.

3) Identification Goaf Based on KANN-DBSCAN: Most hotspots are concentrated within the mining goaf. In-mine hotspots show clustering characteristics, referred to as feature MSs (FMSs), while out-mine hotspots show discrete characteristics as outliers. These outliers pose a significant challenge in target detection. Based on the capability of identifying arbitrary shapes of clustering, the DBSCAN method is used to identify the mining goaf.

The objective of the DBSCAN method is to find the most extensive set of density-connected objects [37]. The determination of the optimal parameters, epsilon (Eps) and minimum points (MinPts), is crucial in the DBSCAN method. Based on the inherent characteristics of the dataset, we obtain the Eps candidate list by calculating the distance matrix of all hotspots and the mean of distance between each hotspot and its nearest neighbor. The distance matrix and the Eps candidate list are then combined to generate the MinPts candidate list. To enhance computational efficiency, it is necessary to perform sampling and interpolation operations [38].

The DBSCAN method is executed to generate clusters that meet the density requirements by checking each FMS to determine if it is a core point [39]. The threshold is set to determine the optimal number of clusters. When the spatial density reaches the maximum and the number of clusters tends to stabilize, the optimal parameters are determined (see Fig. 2). Note that FMSs may not cover the boundary of the mining goaf. This requires both corrosion and buffer operations due to the low density or discontinuity of MSs.

4) Goaf Inversion Based on TLS-PIM: PIM, based on random medium theory, has been widely employed in the mining subsidence field in recent years [3]. Combined with the theory of deep geotechnical mechanics, the equations of mining-induced surface subsidence are listed in Table I to elaborate on the movement of the surface point (x, y).

By analyzing the subsidence information extracted by the IHSA method, we can determine the maximum displacement W_0, the displacements $W_x(x)$ and $W_y(y)$, and the mining ranges L_0 and L_1 in the strike and dip directions. As for the other parameters, the average mining depth H_0 and the thickness of the coal seam m can be found in the regional geological report [40]. Based on the relationship between H_0 and the main influence radius r, we determine the mining depths H_1 and H_2. The dip angle of coal seam α is calculated using (7)

$$\alpha = \arctan[(H_2 - H_1)/L_1]. \quad (7)$$

As the performance of TLS has been demonstrated in similar situations, a fast-converging iterative algorithm [41] is used to solve for the unknown parameters (see Table I) based on the

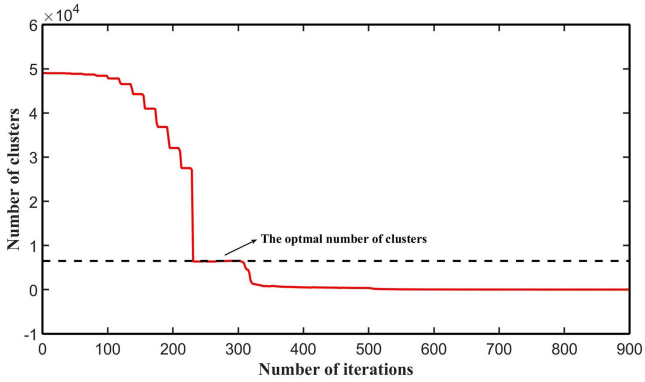

(a)

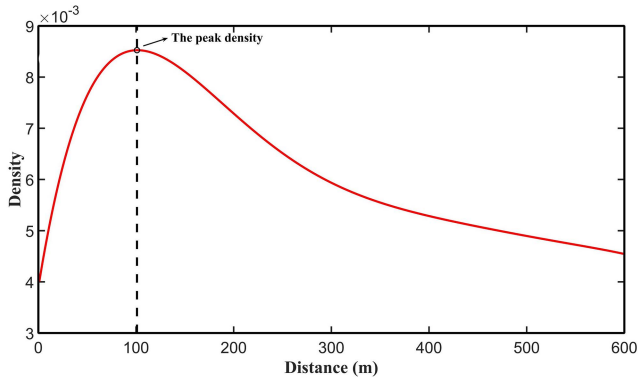

(b)

Fig. 2. (a) Relationship between times and the number of clusters. (b) Relationship between spatial distance and spatial density.

TABLE I
FLOW OF TLS-PIM ALGORITHM

Step 1: $L_0, L_1, \alpha, H_0, H_1, H_2, m, (x, y), W_{\bar{}}$
$q^{(0)}, \tan\beta^{(0)}, S_1^{(0)}, S_2^{(0)}, S_3^{(0)}, S_4^{(0)}, \theta_0^{(0)}$

Step 2:

$$I = L_0 - S_1 - S_2$$
$$L = (L_1 - S_3 - S_4)\cdot\sin(\theta_0 + \alpha)/\sin(\theta_0)$$
$$W_x(x) = \frac{1}{2}\left[erf\left(\sqrt{\pi}\cdot x\cdot\tan\beta/H_0\right) - erf\left(\sqrt{\pi}\cdot(x - I)\cdot\tan\beta/H_0\right)\right]$$
$$W_y(y) = \frac{1}{2}\left[erf\left(\sqrt{\pi}\cdot y\cdot\tan\beta/H_1\right) - erf\left(\sqrt{\pi}\cdot(y - L)\cdot\tan\beta/H_2\right)\right]$$
$$W_0 = m\cdot q\cdot\cos\alpha$$
$$W(x, y) = W_0\cdot W_x(x)\cdot W_y(y)$$
$$\phi^{(i)} = q^{(i)}, \tan\beta^{(i)}, S_1^{(i)}, S_2^{(i)}, S_3^{(i)}, S_4^{(i)}, \theta_0^{(i)}$$
$$\phi^{(i+1)} = \arg\min\left\{\sum_{k=1}^{n}\left(W_k - W(x, y)\right)^2 = \left(X\phi - Y\right)^T\left(X\phi - Y\right)\right\}$$
$$= \left(X^T X\right)^{-1}\left(X^T Y\right)$$

Step 3: repeat step 2 until
$\left\|\phi^{(i+1)} - \phi^{(i)}\right\|_2 = \text{thres}$[1]

[1] thres is the value of the algorithm tolerance

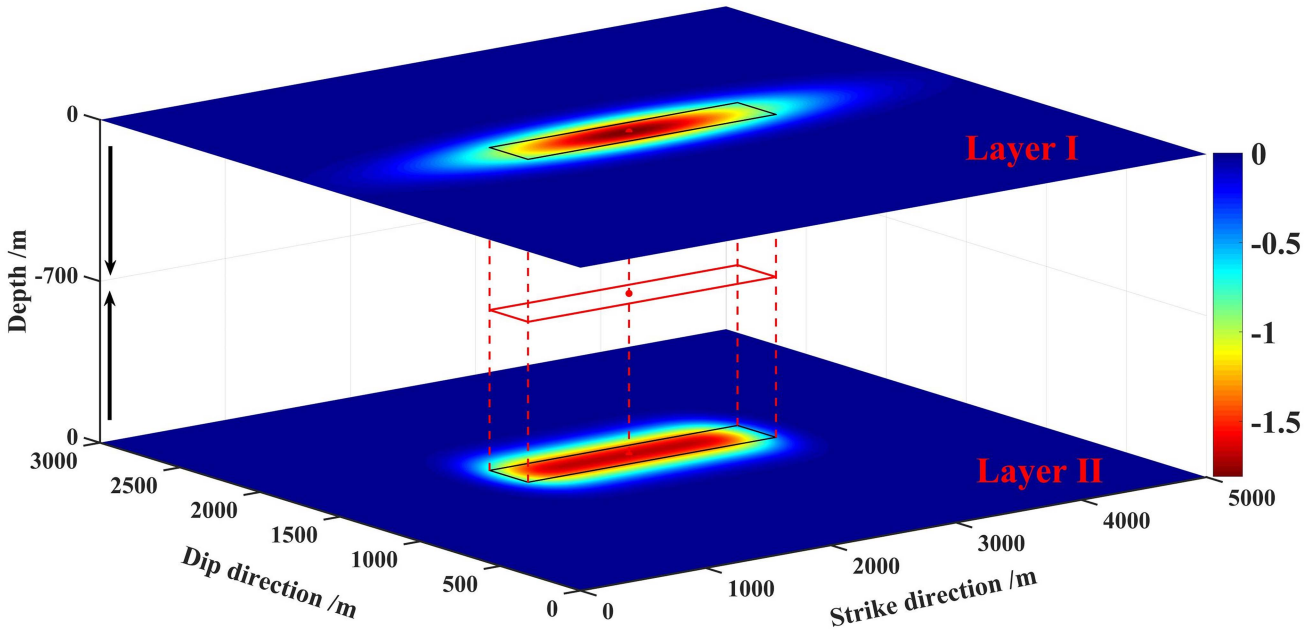

Fig. 3. Simulation results of the mining goaf. Layer I shows the simulated InSAR results caused by mining with the mathematical model. Layer II shows the simulated surface subsidence caused by mining with the TLS-PIM. Black rectangle shows the projection surface of the working face. Red rectangle indicates the actual working face. Red point is the center of the subsidence basin.

criterion of minimizing the objective function

$$\min\left\{\sum_{k=1}^{n}\left(W_k - W(x,y)\right)^2 + \sum_{k=1}^{n}\left(U_k - U(x,y)\right)^2\right\} \quad (8)$$

where W_k and U_k are the deformations in vertical and horizontal directions. Note that the SAR satellites, which fly along the near-polar orbit, contribute very little to LOS measurements in the N-S displacement [42], and therefore, it is not introduced into the model. In addition, the PIM uses the working face coordinate system, where the origin is usually defined at the corner point in the southwest direction of the identified mining goaf. The *X*-axis is along the strike direction of the working face, and the *Y*-axis is along the dip direction perpendicular to the *X*-axis. The operation of coordinate system transformation [43] is used to adjust the position of the working face.

The Guanziling goaf [Area S2 in Fig. 6(a)] is selected as an example for goaf inversion to demonstrate the performance of the TLS-PIM. Fig. 14. shows the simulation results of the Guanziling goaf based on the TLS-PIM.

To verify the effectiveness of the proposed inversion method, 3-D mathematical model [50] was used to simulate the surface subsidence of the mining goaf. The TLS-PIM method was then employed for goaf inversion and compared with the preset parameters.

In this work, the simulated mining depth H_0 was 700 m, the length L_0 was 2000 m, the width L_1 was 250 m, the mining thickness of the coal seam m was 4 m, and the dip angle of coal seam α was 15°. The horizontal size of each model block was 20 m × 20 m, striking a balance between computational efficiency and model accuracy. Fig. 3 shows the location of the simulated goaf. Layer I presents the simulated InSAR results caused by mining with the mathematical model, highlighting the maximum subsidence point situated at the center of the subsidence basin with a maximum settlement of 1.8086 m. Layer II illustrates the simulated surface subsidence caused by mining with the TLS-PIM. A deviation is noticeable between the location of the goaf retrieved by InSAR and the actual location of the working face position, typically aligned with the advance direction of the mining face. It can be concluded that the coal seam was not fully mined.

TABLE II
INVERSION RESULTS AND ERRORS OF GOAF AND PIM PARAMETERS

Parameter	Simulated	Estimated	Absolute Error	Relative Error
L_0	2000	1996.33	3.67	0.18%
L_1	250	250	0.01	0%
α	0.2618	0.2862	0.0244	9.31%
H_1	700	706.44	6.44	0.92%
H_2	700	704.76	4.76	0.68%
m	4	3.72	0.28	7.07%
q	0.9	0.92	0.02	2.48%
$\tan\beta$	2	1.55	0.45	22.59%
θ_0	1.3	1.21	0.09	6.69%

The parameters estimated by the TLS-PIM method are listed in Table II. Among those length parameters (L_0, L_1, H_1, H_2, m), the maximum value of relative error is 7.07% in the mining thickness of the coal seam m with an absolute error of 0.28 m. The maximum value of absolute error is 6.44 m in the uphill direction of the mining depth H_1. The strike direction

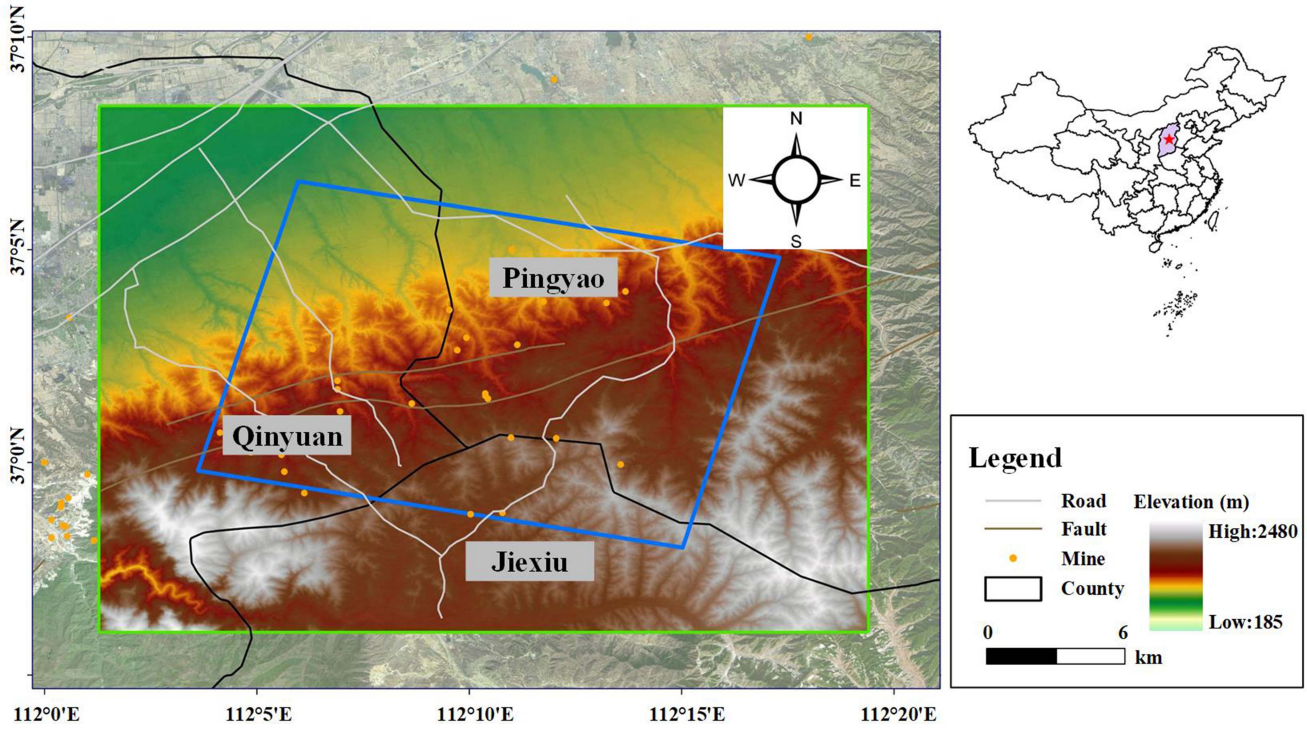

Fig. 4. Location of the study area and data coverage, with optical image as the base map. Blue rectangle represents the coverage of the RADARSAT-2 images.

exhibits a deviation compared with the dip direction. The reason for this issue is that the InSAR results show a wider subsidence extent in the strike direction, resulting in an overestimation of the parameters. Compared with the simulated parameters, estimated mining length and width exhibit slight fluctuations. Among those angle parameters (α, $\tan\beta$, θ_0), the maximum value of absolute error is 22.59% of the tangent of the main influence angle $\tan\beta$, with an absolute error of 0.45. As the dip angle of coal seam α increases, the tangent of the main influence angle $\tan\beta$ decreases, in accordance with the simulation results. The subsidence coefficient q has a relative error of 2.48% and an absolute error of 0.02, showing a slight deviation.

The simulation experiment demonstrates the feasibility of the proposed inversion method. The subsidence information of the goaf extracted from the IHSA method contributes to the acquisition of the parameters required by the PIM and the improvement of goaf inversion capability.

B. Study Area

The study area is located in Wuxiang, Shanxi Province, China, characterized by predominantly hilly terrain with elevation range between 185 and 2480 m, covering an area of 224 km^2. The region is rich in mineral resources and was once listed as one of the 100 vital coal-producing counties in China, with coal reserves of 180 million tons. Unfortunately, coal mining activities have caused severe geological hazards, such as road collapses and land cracks [43], posing a serious threat to lives and properties. Severe ground subsidence has forced the entire town to relocate to a new settlement in 2018. Geologically, the study area falls within the Permian, specifically the upper Shihezi Formation and the Sunjiagou Formation [44]. In addition, there exist a positive fault 2.65 km north of the Guanziling goaf with a length of 40 km and a width of 2 km, including four parallel diagonal grabens and a horst in the western region (see Fig. 4).

TABLE III
KEY PARAMETERS OF RADARSAT-2 SAR IMAGES

Parameters	Description
Sensor	RADARSAT-2
Acquisition Time	2018.03–2018.11
Number of Images	10
Incidence Angle	27.6593°
Ground Resolution / (m) (Rg × Az)	2.66 × 3.03
Multilooking	2:4
Number of Interferograms	24

C. Datasets

This study leverages ten RADARSAT-2 SAR images to generate interferometric pairs. The spatial coverage of the SAR images is illustrated in Fig. 4. Key parameters of SAR images are listed in Table III. The image acquired on 27 August, 2018, serves as the reference image for resampling other images. The distribution of spatial-temporal baseline is illustrated in Fig. 5. The shortest, longest, and average spatial baselines are 1.184, 357.892, and 150.623 m, respectively. The corresponding

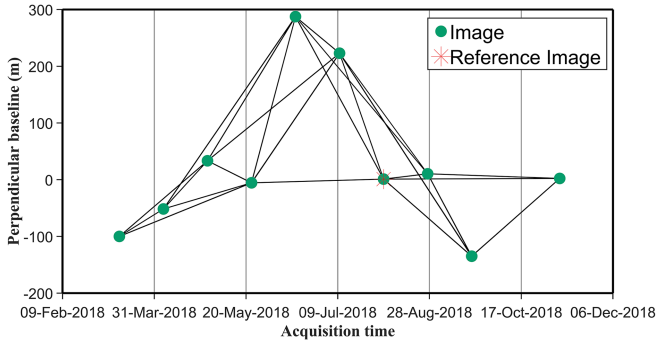

Fig. 5. Spatial-temporal baseline of interferogram pairs.

temporal baselines exhibit the following values: 24 days (shortest), 96 days (longest), and 49 days (average). In addition, a one-arc-second gridded AW3D30 DEM [45] has been prepared for further processing.

III. Results and Analysis

A. InSAR Deformation Results

Based on the coherence coefficient and amplitude deviation methods, 1 317 873 MSs are extracted from the SAR dataset, resulting in a spatial density of approximately 5885 MSs/km^2 (Note: in urban areas, the typical density is greater than 150 MSs/km^2). These MSs are widely distributed across roads, cliffs, and the mining area. The large number of MSs is beneficial for full coverage of the mining area. The annual deformation rate map derived by TS-InSAR is shown in Fig. 6. The color bar in the map represents the motion direction relative to the satellite along the LOS. Negative values (red color) indicate movement away from the satellite, while positive values (depicted in blue) indicate movement closer to the satellite. The deformation rate ranges from -0.244 to 0.118 m/year while the cumulative deformation ranges from -0.154 to 0.092 m.

In the study area, the two largest mining goafs are Area 11 (referred to as S1), covering 1.119 km^2, and Area 9 (referred to as S2), covering 1.487 km^2, respectively. Area S3, which includes six mining goafs with distinct extents and mining conditions, represents the most complicated environment within the study area and provides an ideal setting for assessing the performance of the IHSA method. Area S1 is situated in the northeast of Taishangou. Area S2 is located near Guanziling.

Moreover, the distribution histograms of MSs within stable regions are calculated for accuracy assessment [46], [47], as illustrated in Fig. 7. Fig. 7(a) shows an average deformation rate of -0.31 cm/year with a standard deviation of 1.4 cm/year. Fig. 7(b) shows an average cumulative deformation of -0.14 cm with a standard deviation of 0.8 cm. The larger standard deviations are attributed to the environment characteristics of the study area: atmospheric effect and spatial-temporal decorrelation.

B. Mining Goaf Identification Results

The HSA-RISA method is performed on all MSs using a threshold of ± 1.96 for the Z-score and a threshold of 95% for the P-value to extract 49 038 candidate FMSs with strong clustering characteristics. These FMSs are mainly situated within the goaf. The outliers are further eliminated using the KANN-DBSCAN method, resulting in the identification of 25 deformation zones with a total of 47 656 MSs (see Fig. 8).

The location of the working face inversed by InSAR results exhibits a slight deviation from the actual working face [2]. Considering geological conditions and prior experience, feature points, such as inflection points and boundary points, are moved towards the strike direction to determine the goaf boundary. In engineering surveying, -10 mm is used as the threshold to determine the boundary [2]. Based on the acknowledgement that weighted averaging can partly reduce the measurement errors of InSAR results, a threshold of an annual average subsidence rate of -10 mm/year is set and the discontinuous boundaries are connected through visual interpretation to determine the reference goaf boundary, i.e., the red rectangles in Fig. 8.

Based on the time series cumulative deformations identified by the IHSA method, a threshold of -10 mm for the cumulative deformation of each period is set to determine the dynamic subsidence boundary during the observation period, i.e., the gradient red lines in Fig. 9. The evolving subsidence boundaries of two mining goafs, Areas S1 and S2, are shown in Fig. 9(a) and (b), respectively.

Area S1, the Taishangou goaf, exhibited a gradual expansion from north to south during the observation period and continues to expand southward. The maximum deformation rate recorded is -0.213 m/year, with the maximum cumulative deformation of -0.141 m. Area S2, the Guanziling goaf, with the maximum deformation rate of -0.226 m/year, exhibited a gradual expansion from the center to the surrounding during the observation period. The subsidence range gradually expands from 0.71to 1.48 km^2, and the depth of subsidence increases. The maximum cumulative deformation ranges from -0.029 to -0.154 m. Notably, villages are situated on the south, northeast, and northwest sides of Area S2. Optical images, deformation rate map, and time-series deformation maps are used to interpret the identified deformation zones. Among the 24 identified mining goafs, 8 of them (2, 5, 9, 10, 13, 17, 21, and 24) pose a threat to nearby villages (see Fig. 10).

It is worth mentioning a slight deformation in the southwestern part of the study area. Upon examination of optical images, it is observed that the area is characterized by steep mountainous terrain with terraced fields, and no mining activities take place. On the northeast side of the enlarged image, ground subsidence is induced by construction activities. Therefore, it is concluded that the slight deformation is a result of construction activities and geological hazards, such as landslides. This serves to validate the ability of the IHSA method to identify zones at risk of geological hazard.

To assess the performance of the IHSA method, we compare it with other methods, including the iterative threshold segmentation (ITS) method [48], regional growth (RG) method [49], optimized hotspot analysis (OHSA) [20], and HSA-RISA method (see Fig. 11). We considered five indicators: the number of extracted MSs, the number of in-mine MSs, the number of outliers, extraction accuracy (the number of in-mine MSs / the number of all in-mine MSs), and identification accuracy (the

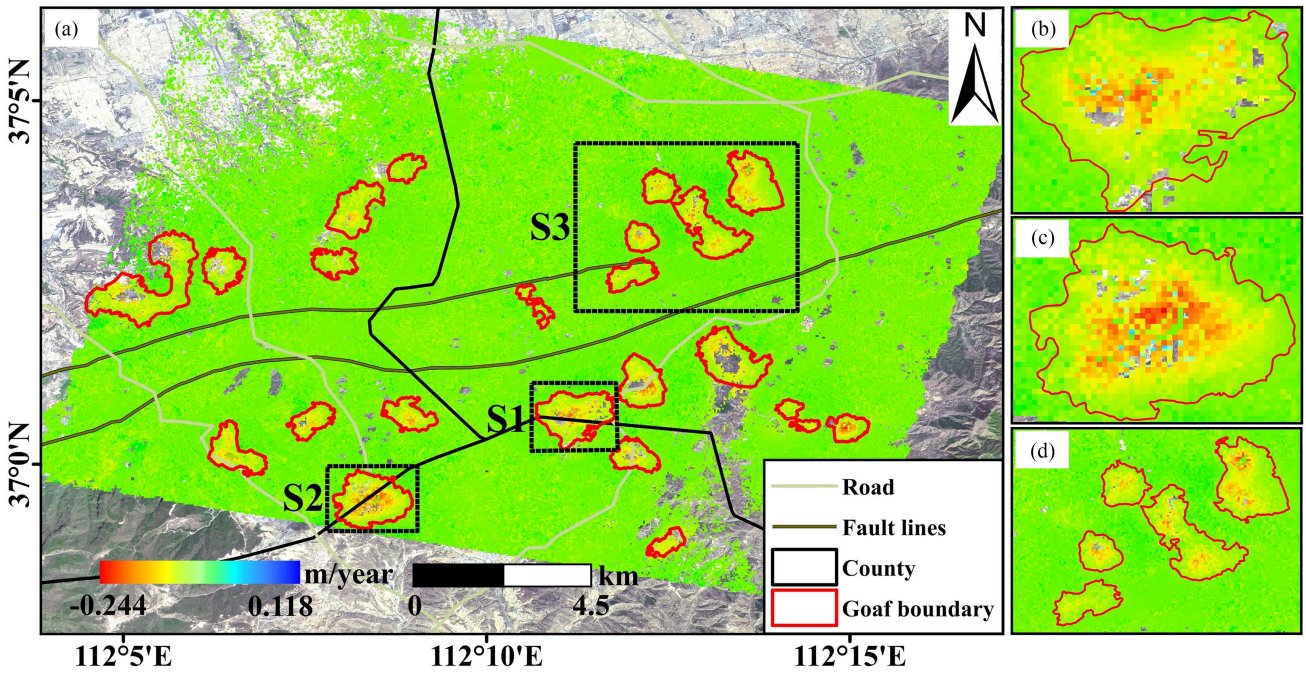

Fig. 6. (a) Annual deformation rate of Changzhi from March 2018 to November 2018. Red solid rectangles represent the goaf boundaries. Black dashed rectangles represent the boundaries of the county. (b)–(d) Enlarged views of Areas S1–S3.

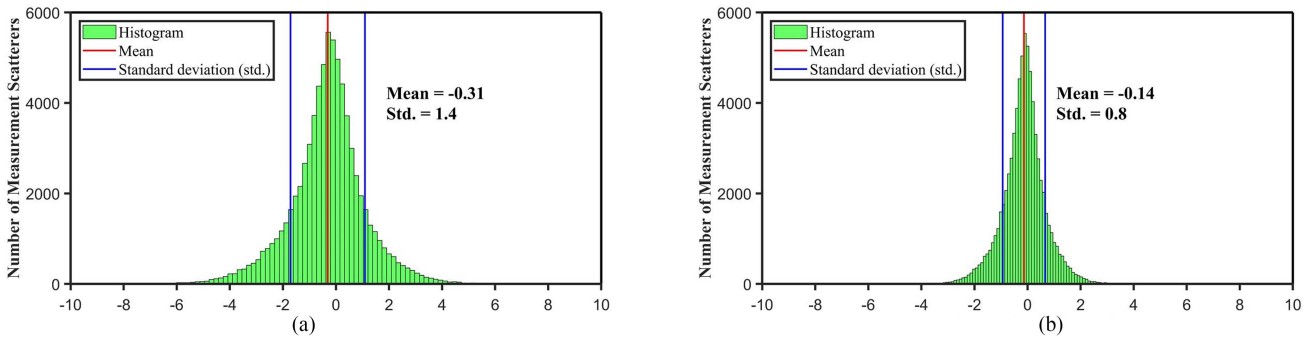

Fig. 7. Accuracy assessment of LOS deformation maps. (a) Distribution histogram of LOS deformation rate. (b) Distribution histogram of LOS cumulative deformation.

number of in-mine MSs / the number of extracted MSs). Based on the reference goaf boundary determined by a threshold of −10 mm/year and visual interpretation, 102 489 out of the 1 317 873 MSs derived by InSAR are classified as in-mine MSs. The identification results for the entire area and Area S3 are presented in Figs. 11 and 12, respectively. The corresponding statistical results are listed in Tables IV and V, respectively.

The RG method identified many in-mine MSs, albeit at the cost of a corresponding number of outliers. Comparing Fig. 11(a) and (e), the results from the ITS method resemble those of the IHSA method's method; however, they exhibit lower density and accuracy in the interpolation of MSs to generate the raster image. The OHSA method yields results with a small number of outliers despite the lower quantity and coverage, as seen in Areas 1, 2, 7, 11, 13, 14, 20, and so forth. Fig. 11(e) shows the results from density-based spatial clustering following the HSA-RISA method. The IHSA method automatically eliminates outliers and performs spatial clustering of MSs, resulting in fewer outliers, specifically 797. Furthermore, there are no outliers in the Area S3 [see Fig. 12(e)]. The IHSA method reaches the highest identification accuracy for the entire study area and Area S3, measuring at 98.328% and 100%, respectively. In conclusion, the results demonstrate the superior performance of the IHSA method in identifying geological hazard risk zones.

C. *Spatial-Temporal Evolution Characteristics Analysis*

Guanziling Goaf, Area S2, is selected for the study of the spatial-temporal evolution characteristics of the mining goaf due to its extensive subsidence coverage, continuous subsidence boundaries for calculating parameters required by the PIM method, and a higher density of monitoring points

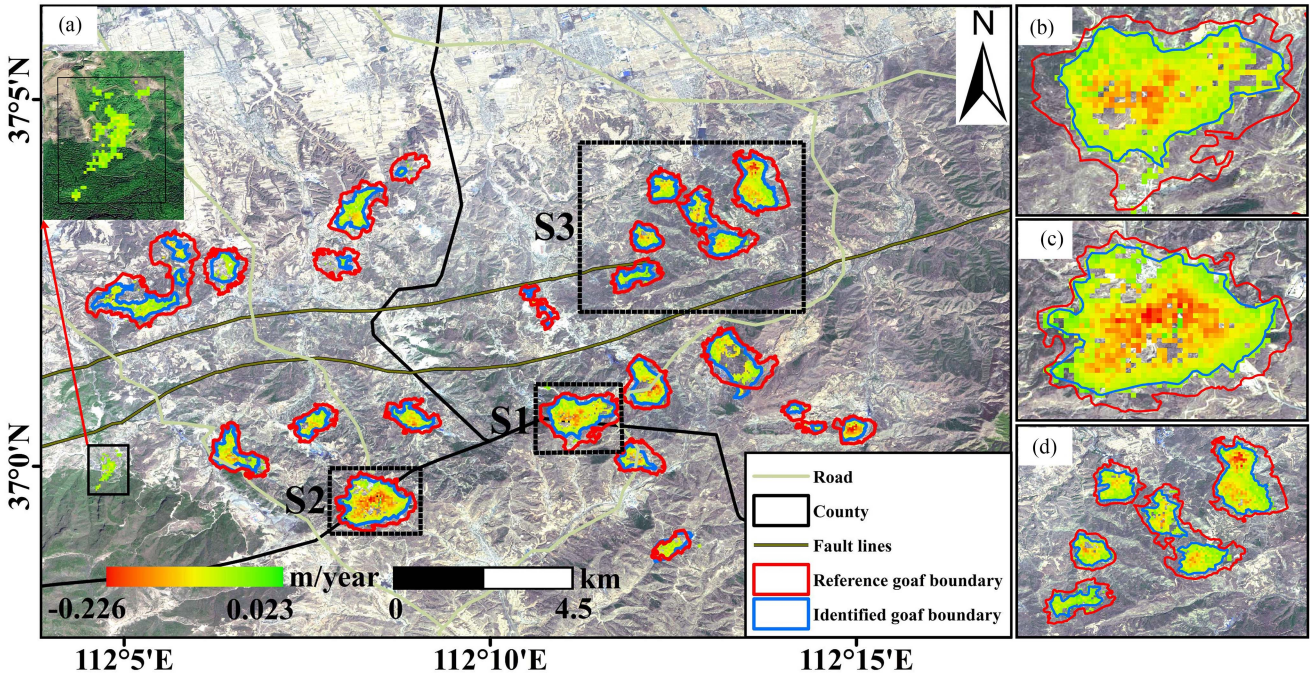

Fig. 8. (a) Annual deformation rate of Changzhi identified by the IHSA method from March 2018 to November 2018. Red rectangles represent the reference goaf boundaries. Blue rectangles represent the identified goaf boundaries. (b)–(d) The enlarged views of Area S1, S2, and S3.

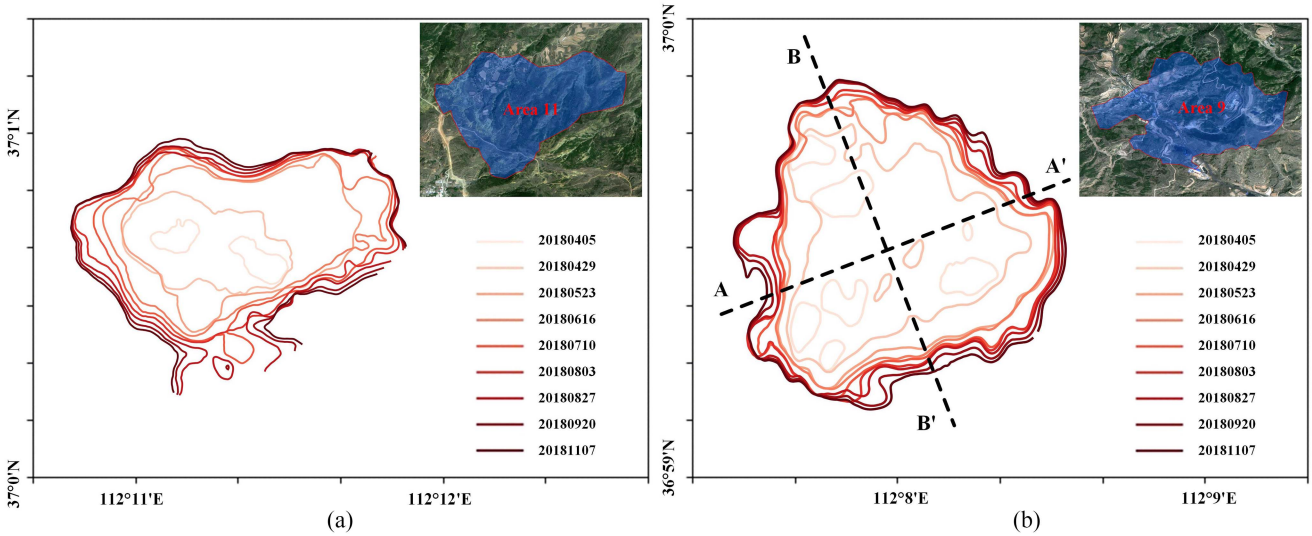

Fig. 9. (a) and (b) Dynamic subsidence boundaries of the mining goaf from March 2018 to November 2018 of Area S1 and S2, respectively. Red lines represent the dynamic subsidence boundaries of the mining goaf that changes with the acquisition time of images. Dashed line AA' and BB' represent the strike and dip directions of Area S2 in (b), respectively.

TABLE IV
COMPARISON OF THE DIFFERENT METHODS WITHIN THE ENTIRE STUDY AREA

Methods	Number of extracted MSs	Number of in-mine MSs	Number of outliers	Extraction accuracy	Identification accuracy
ITS	42 791	36 641	6150	35.751%	85.628%
RG	128 483	64 367	64 116	62.804%	50.098%
OHSA	31 565	30 459	1106	29.719%	96.496%
HSA-RISA	49 038	46 916	2122	45.777%	95.673%
IHSA	47 656	46 859	797	45.721%	98.328%

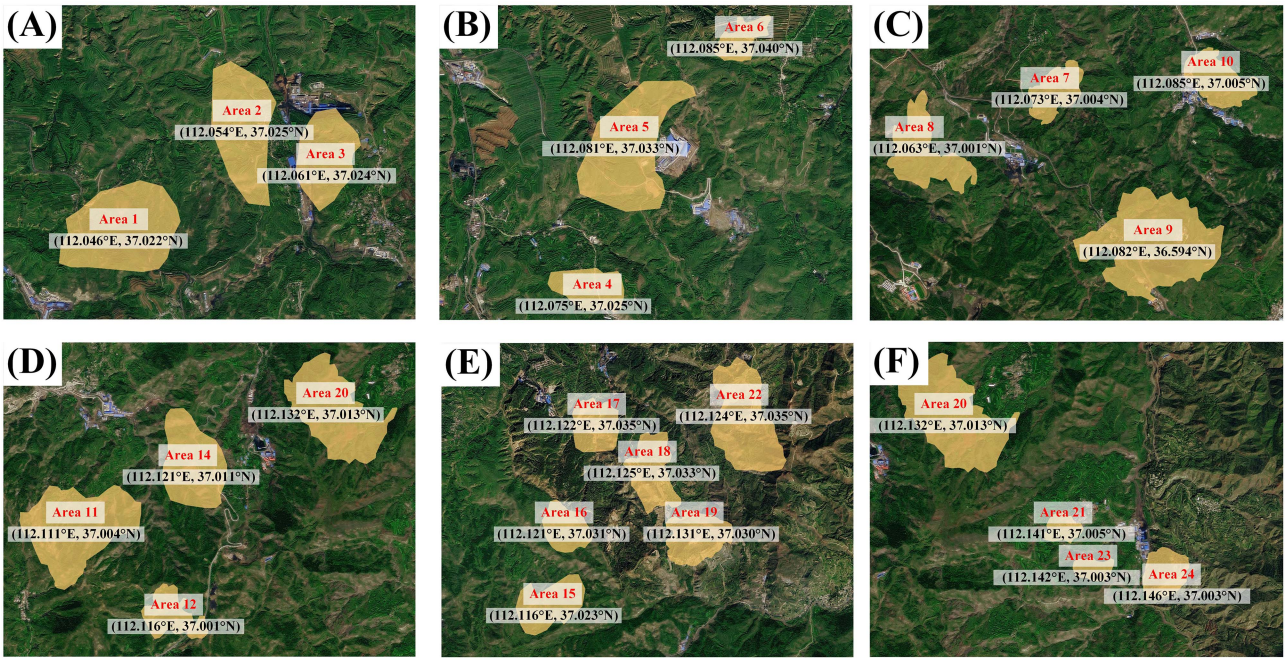

Fig. 10. (a)–(f) Optical image of the identified mining goafs. Yellow rectangles represent the range of the identified mining goafs.

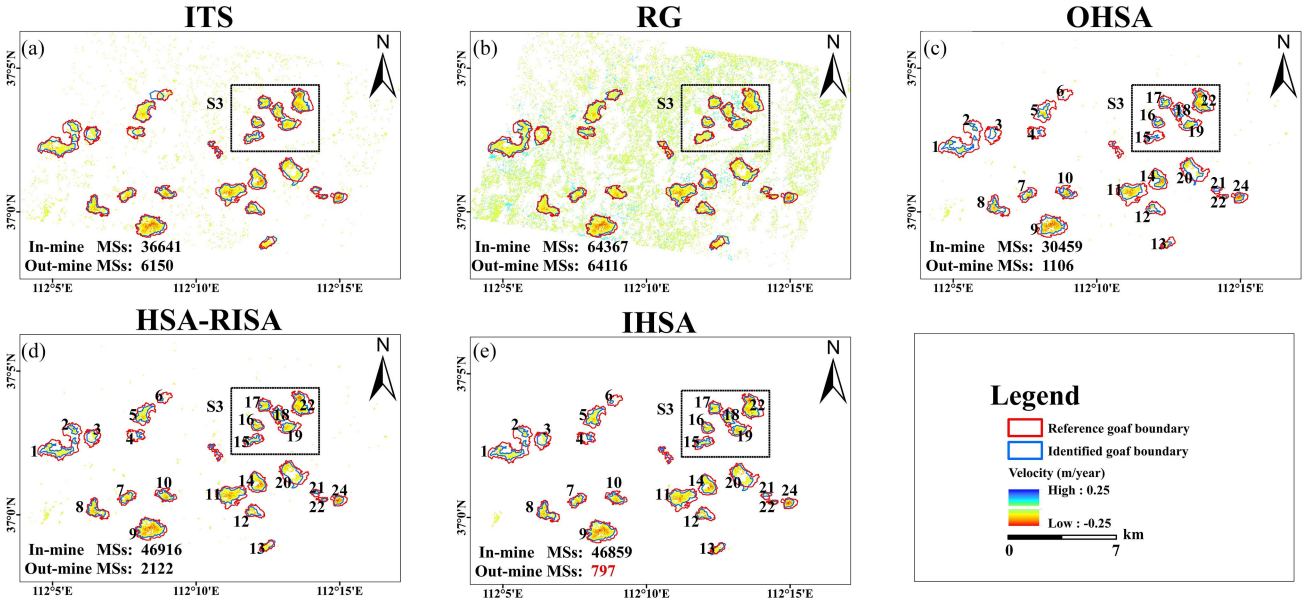

Fig. 11. Comparison of identification results of the ITS, RG, OHSA, HSA-RISA, and IHSA methods. Red rectangles represent the reference goaf boundaries. Blue rectangles represent the identified goaf boundaries. Enlarged views of the identification results for Area S3 are shown in Fig. 12.

(1016.1 MSs/km^2) compared to Area 11 (985.17 MSs/km^2). The goaf is located in Lianfu Town, Jiexiu City, Shanxi Province, about 1.6 km from east to west and 1.4 km from north to south.

Based on the identified subsidence information, the dynamic subsidence of the mining goaf in Area S2 is clearly illustrated in Fig. 9(b). Based on the TLS-PIM, the relationship between underground movement and ground subsidence is established (see Fig. 14). The inversion results of the mining goaf based on the TLS-PIM method are given in Table VI.

During the observation period, the surface above the coal mine gradually subsided, ranging from −29.13 to −153.58 mm, and the affected range gradually expanded from 0.71 to 1.48 km^2. The subsidence coefficient representing the ratio of surface deformation to the thickness of coal seam, is affected by factors

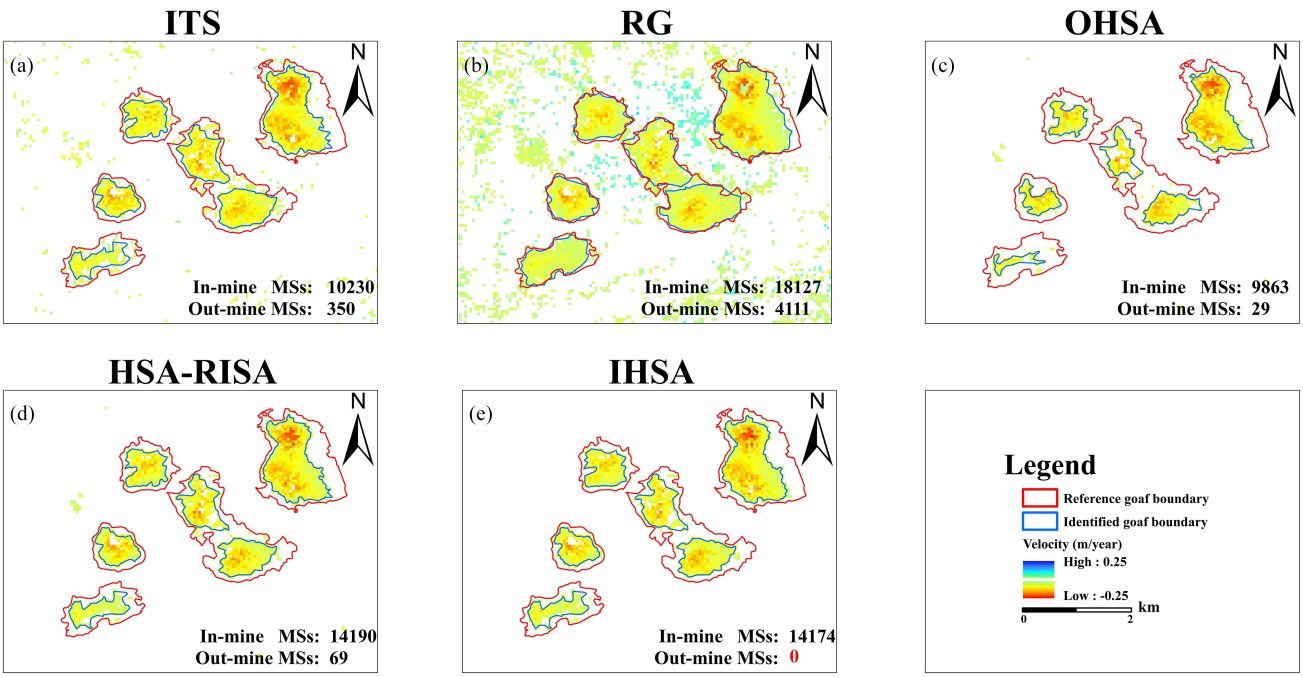

Fig. 12. Comparison of identification results of the ITS, RG, OHSA, HSA-RISA, and IHSA methods, in Area S3. Red rectangles represent the reference goaf boundaries. Blue rectangles represent the identified goaf boundaries.

TABLE V
COMPARISON OF THE DIFFERENT METHODS WITHIN THE AREA S3

Methods	Number of extracted MSs	Number of in-mine MSs	Number of outliers	Extraction accuracy	Identification accuracy
ITS	10 580	10 230	350	35.829%	96.692%
RG	22 238	18 127	4111	63.488%	81.514%
OHSA	9892	9863	29	34.544%	99.707%
HSA-RISA	14 259	69	2122	49.700%	99.516%
IHSA	14 174	14 174	0	49.643%	100.000%

TABLE VI
RESULTS OF THE MINING GOAF BASED ON THE TLS-PIM

Parameters	Values
Longitude (°)	112.08
Latitude (°)	36.59
Length (m)	561.52
Width (m)	411.28
Depth (m)	584.64–638.23
Subsidence coefficient	0.1–0.8
Deviation of inflection point (m)	94
Thickness of the coal seam (m)	5.3
Dip angle of coal seam (°)	15.0
Area (km^2)	1.48
Maximum cumulative deformation (m)	-0.154
Maximum deformation velocity (m/year)	-0.255

such as the lithology of the strata above the coal seam, mining depth, the extent of the working face, and so on. A positive fault, located 2.65 km north of the Guanziling goaf, triggered heterogeneous subsidence of the above strata due to the excavation of the coal seam. With the continued excavation, the main influence radius increases, along with the depth of the coal seam. Insufficient mining results in a smaller calculated mining depth.

However, inaccurate estimation of the subsidence information within the mining goaf can partially affect the simulation results of the model. We consider two situations: one involving underestimation (reducing the length and width of the working face by 20 m) and the other involving overestimation (increasing the length and width of the working face by 20 m). These estimated parameters are both utilized as input for the TLS-PIM in goaf inversion. In addition, the 3-D mathematical modeling method of the subsidence basin in the mining area [50] can be established for comparison. Along the strike and dip directions (AA' and BB') [see Fig. 9(b)], cumulative deformation on November 07 is selected for comparison between InSAR measurements and simulation results using five methods: the Curve fitting, the TLS-PIM, the Math Model, the Poor-PIM, and the Rich-PIM (see Fig. 15 and Table VII). The profiles exhibit slight

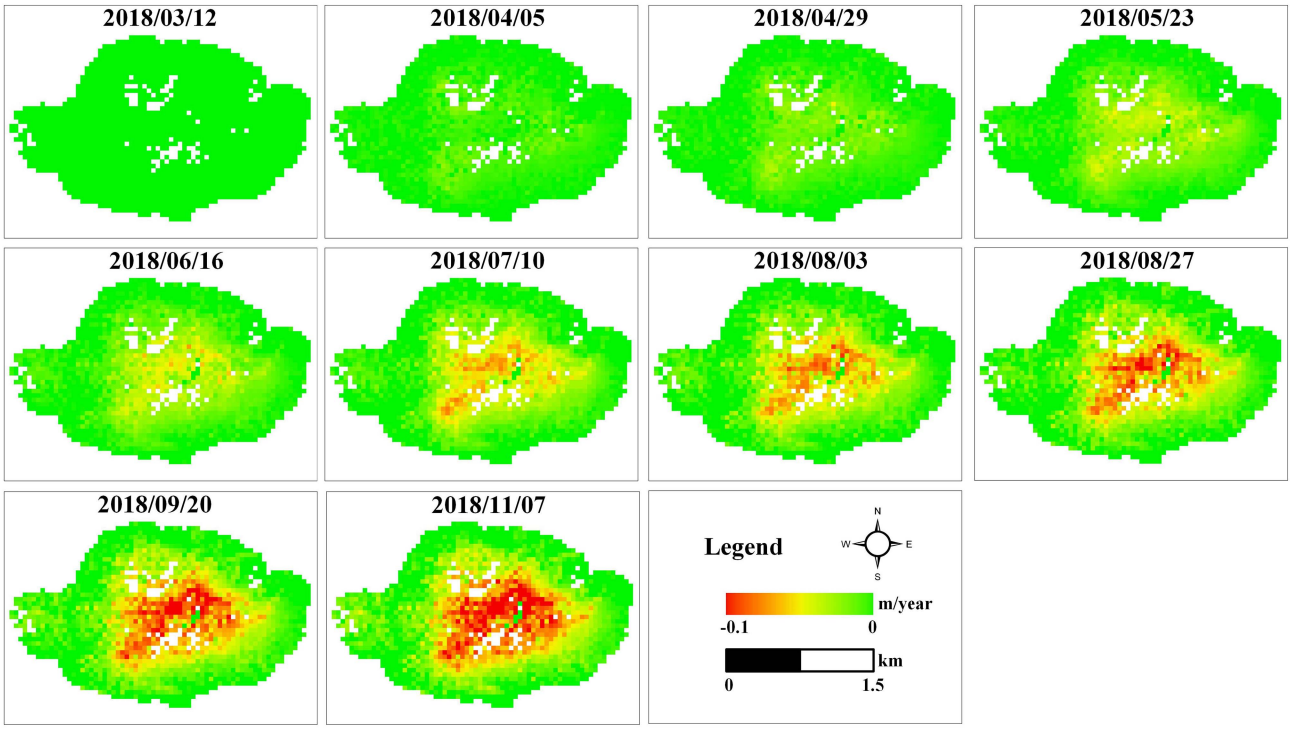

Fig. 13. Time series diagrams of ground subsidence identified by the IHSA method in Area S2 from March 2018 to November 2018.

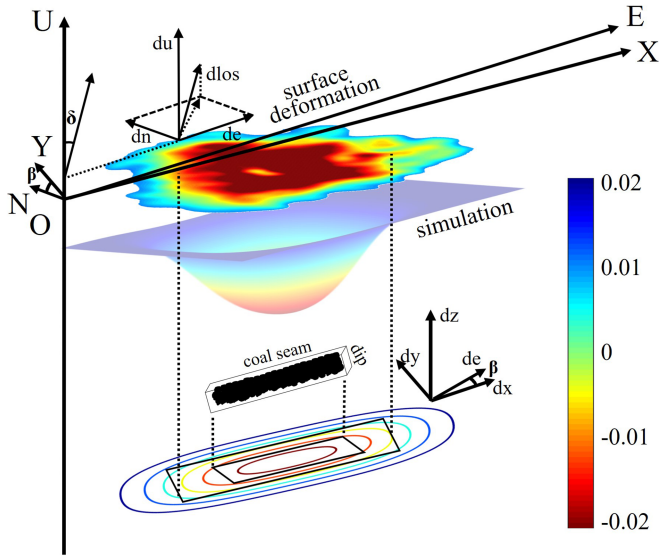

Fig. 14. Relationship between the identified surface deformation and simulated mining goaf. O-NEU is the working face coordinate system. O-XYU is the geographic coordinate system.

differences among the five simulation results. Table VII tabulates that the correlation of curve fitting in the strike direction is higher compared with others. However, the curve fitting method, based on the least-squares polynomial fitting, is optimal for one profile, but not applicable to others, and does not conform to the subsidence patterns of coal mining. The TLS-PIM method

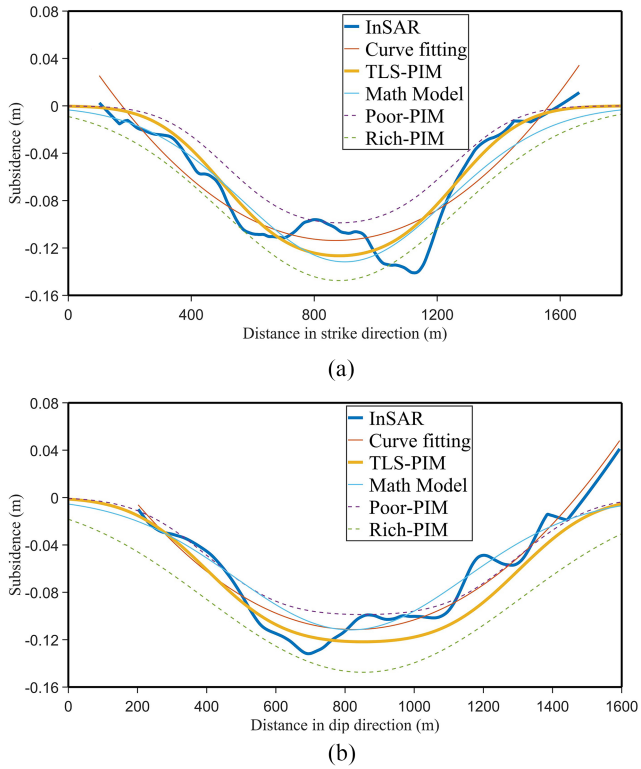

Fig. 15. Profiles of the simulated deformation model. Blue line is the profile of the TS-InSAR. Yellow line is the profile of the TLS-PIM. They are drawn in the strike and dip directions, (a) and (b), respectively.

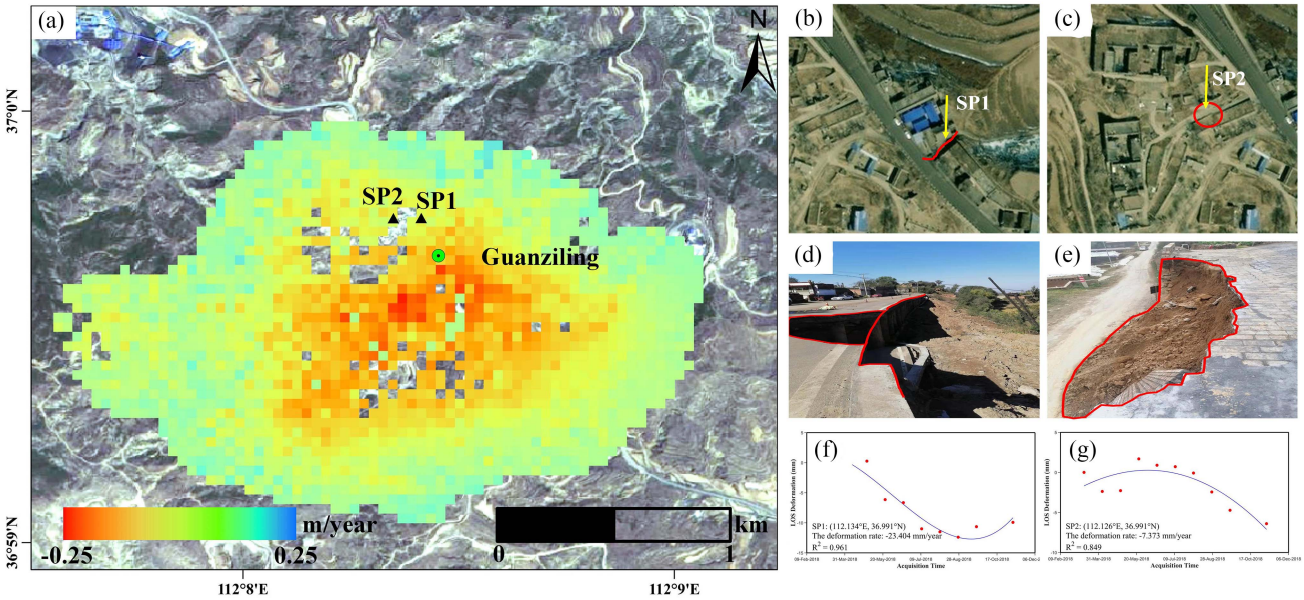

Fig. 16. (a) Location and the results of field investigation of two places, SP1 and SP2, in the Guanziling area. (b) and (c) Location of two places in the optical images. (d) and (e) Results of field investigation of two places. (f) and (g) Cumulative displacement of the TS-InSAR of SP1 and SP2, respectively.

TABLE VII
COMPARISON OF FITTING RESULTS OF DIFFERENT METHODS

Correlation	Strike direction	Dip direction
Curve fitting	85.58%	92.62%
TLS-PIM	89.32%	83.38%
Math model	62.85%	56.58%
Poor-PIM	73.25%	40.91%
Rich-PIM	63.08%	72.95%

considers the subsidence information from multiple directions within the mining goaf for overall optimization, aligning with the subsidence patterns of coal mining.

The simulation results of the Poor-PIM and the Rich-PIM both exhibit a lower correlation with InSAR measurements in two directions compared with the TLS-PIM method. The Math Model, following the mathematical modeling method of the subsidence basin, faces difficulty in inverting the actual subsidence of the mining goaf with correlation coefficients of 0.6285 and 0.5658, respectively. The significant differences lie in the maximum subsidence magnitude and the sink width. The maximum deviation between the results of InSAR and the TLS-PIM is 0.0409 m at 1041 m in the strike direction. The mean error is −0.0024 m, the rms is 0.0152 m with a correlation coefficient of 0.8932. In the dip direction, the maximum deviation is 0.0468 m at 697 m. The mean error is 0.0119 m, the rms is 0.0179 m with a correlation coefficient of 0.8338. Compared with the results of the TLS-PIM, the InSAR-derived results indicate greater depth, which may be attributed to geological formations, such as faults.

The results demonstrate the superiority of the TLS-PIM compared with other methods, highlighting the significance of accurately acquiring subsidence information of the mining goaf.

D. Field Investigations

Field investigations were conducted in the Guanziling area, i.e., Area S2 as shown in Fig. 6(a). The survey revealed that severe surface subsidence due to excessive coal mining has disrupted the original stress balance of the surrounding rock mass and led to geological hazards, such as collapse pits and subsidence basins, posing a potential threat to villages and necessitating their relocation.

Two feature places, SP1 and SP2, are selected in the Guanziling area. A buffering zone of 200 m was applied to the results identified by the IHSA method. It serves as the displacement base map to cover the edge zones of the mining goaf, as illustrated in Fig. 16. SP1 is located 15 m to the east side of County Road X923 at the edge of the goaf [see Fig. 16(b)]. The bottom of the road has been hollowed out and supported by coal pillars, as shown in Fig. 16(d). SP2 is located 50 m to the west side of County Road X923 [see Fig. 16(c)], with large cracks in the road, sinking and collapsing foundation edges, as is shown in Fig. 16(e).

These two feature points are positioned at the edge of the mining subsidence area, with low coherence and sparse monitoring point density. The variety of ground targets in these pixels contributes to unstable echo signals, disruptions to the acquisition of phase information and significant fluctuations in the time-series deformations. We fitted the time-series deformations of these two feature points using polynomials. The time-series deformations of SP1 and SP2 are depicted in Fig. 16(f) and (g). Meanwhile, the correlation coefficient between the fitting results and cumulative deformation is calculated to reflect the subsidence trend. The correlation coefficient of SP1 is 0.961, and the maximum settlement is −12.391 mm. The correlation coefficient of SP2 is 0.849, and the maximum deformation is −6.403 mm. The unstable foundation and the

coal pillars supporting the road contribute to the more severe subsidence at SP1.

IV. Discussion

With the advancement of InSAR technology and the accumulation of SAR images, it has become easier to acquire millimeter-level surface deformation on a broad scale. However, due to the complex monitoring environments and large coverage areas, the automatic extraction of valuable information from InSAR results remains a challenging task. HSA is used to quantify the spatial dependence, facilitating the identification of potential risk areas. Based on the statistical characteristics of the dataset, the article proposes an effective approach for determining the optimal search distance through the incorporation of iterative strategy and incremental spatial autocorrelation. The KANN-DBSCAN method has the advantage of dividing areas with a sufficient density of points into clusters to identify in-mine MSs.

However, most of mines are affected by temporal and spatial decoherence, which leads to incomplete coverage of the mining goaf in the InSAR results. The sparse density of MSs may cause a smaller identified area than the actual goaf, as presented in Area 5 and Area 13, and the occurrence of the cavity in mining goaf, as presented in Area 20. Our identification method may merge relatively close mining goafs, such as Area 8 and Area 22, which also evident in the results of other identification methods we compared. Both erosion and buffering operations are necessary for the complete coverage of the mining goaf.

The deformation information extracted from the IHSA method contributes to the determination of the optimal parameters required by the PIM. Simulation experiments were conducted to verify the effectiveness of the proposed inversion method. To emphasize the significance of accurate working face parameters, with the Guanziling goaf as an example, we expanded and reduced the working face scope by 20 m, resulting in two scenarios: Poor-PIM and Rich-PIM. We also compared the simulation results of the 3-D mathematical model. The significant correlations of 89.32% and 83.38% observed in both the strike and dip directions underscore the superiority of the TLS-PIM method.

In addition, it is worth mentioning that ground deformation is only one factor of risk, and the assessment of geological hazard risk typically requires careful consideration of multiple factors, such as geological structure, historical events, population density, and land use.

V. Conclusion

Mining activities disrupt the natural stress balance of surrounding rock formations and cause severe damage to surface structures and farmlands. Therefore, it is of great practical significance to understand the spatial-temporal evolution characteristics of mining goaf.

In this article, we design a comprehensive workflow for the automatic spatial-temporal evolution inversion of mining goaf. First, TS-InSAR is utilized to generate the surface deformation of the mining area. Then, based on the spatial statistics and clustering characteristics of MSs, we propose an IHSA to automatically identify mining goaf. This method combines HSA with recursive incremental spatial autocorrelation and KANN-DBSCAN for spatial clustering. Finally, based on the deformation information of the mining goaf extracted by the IHSA method, the TLS-PIM is employed to perform goaf inversion. The proposed workflow is successfully applied to the Wuxiang area in Shanxi province, with a total of 24 goafs identified, eight of them threatening villages. In addition, the Guanziling goaf is selected for the spatial-temporal evolution inversion. We have compared the IHSA method with four methods using five indicators, and likewise, we have compared the TLS-PIM method with four methods in terms of their correlation with the InSAR results in the strike and dip directions. Furthermore, field investigations were carried out. The results demonstrated the superiority of our method and supported the geological hazard investigation and mine safety supervision department.

The next step in our plan is to introduce distributed scatterers and Gaussian kernel functions to cover the areas with sparse density of MSs.

Acknowledgment

The authors would like to thank the Canadian Space Agency for providing RADARSAT-2 data and the Japan Aerospace Exploration Agency for providing AW3D30 DEM data.

References

[1] J. Lu, C. B. Jiang, Z. Jin, W. S. Wang, W. J. Zhuang, and H. Yu, "Three-dimensional physical model experiment of mining-induced deformation and failure characteristics of roof and floor in deep underground coal seams," *Process. Saf. Environ. Protection*, vol. 150, pp. 400–415, Apr. 2021, doi: 10.1016/j.psep.2021.04.029.

[2] Y. P. Xia and Y. J. Wang, "InSAR- and PIM-based inclined goaf determination for illegal mining detection," *Remote Sens.*, vol. 12, no. 23, Dec. 2020, Art. no. 3884, doi: 10.3390/rs12233884.

[3] M. Y. Shi, H. L. Yang, B. C. Wang, J. H. Peng, Z. Z. Gao, and B. Zhang, "Improving boundary constraint of probability integral method in SBAS-InSAR for deformation monitoring in mining areas," *Remote Sens.*, vol. 13, no. 8, Apr. 2021, Art. no. 1497, doi: 10.3390/rs13081497.

[4] Z. Y. Wang et al., "Monitoring, analyzing, and modeling for single subsidence basin in coal mining areas based on SAR interferometry with L-band data," *Sci. Program.*, vol. 2021, Feb. 2021, Art. no. 6662097, doi: 10.1155/2021/6662097.

[5] P. F. Ma, Y. Zheng, Z. J. Zhang, Z. R. Wu, and C. Yu, "Building risk monitoring and prediction using integrated multi-temporal InSAR and numerical modeling techniques," *Int. J. Appl. Earth Obs. Geoinf.*, vol. 114, Nov. 2022, Art. no. 103076, doi: 10.1016/j.jag.2022.103076.

[6] F. F. Liu, X. Z. Fan, T. Zhang, and Q. H. Liu, "GNSS-Based SAR interferometry for 3-D deformation retrieval: Algorithms and feasibility study," *IEEE Trans. Geosci. Remote Sens.*, vol. 56, no. 10, pp. 5736–5748, Oct. 2018, doi: 10.1109/TGRS.2018.2825220.

[7] Q. L. Luo, G. Q. Zhou, and D. Perissin, "Monitoring of subsidence along Jingjin inter-city railway with high-resolution TerraSAR-X MT-InSAR analysis," *Remote Sens.*, vol. 9, no. 7, Jul. 2017, Art. no. 717, doi: 10.3390/rs9070717.

[8] M. Genis, H. Akcin, O. Aydan, and G. Bacak, "Investigation of possible causes of sinkhole incident at the Zonguldak Coal Basin, Turkey," *Geomech. Eng.*, vol. 16, no. 2, pp. 177–185, Oct. 2018, doi: 10.12989/gae.2018.16.2.177.

[9] Q. X. Tao, F. Y. Wang, Z. J. Guo, L. Y. Hu, C. Yang, and T. W. Liu, "Accuracy verification and evaluation of small baseline subset (SBAS) interferometric synthetic aperture radar (InSAR) for monitoring mining subsidence," *Eur. J. Remote Sens.*, vol. 54, no. 1, pp. 641–662, Jan. 2021, doi: 10.1080/22797254.2021.2002197.

[10] W. H. Zhang, J. C. Shi, H. W. Yi, Y. Zhu, and B. Xu, "Underground goaf parameters estimation by cross-iteration with InSAR measurements," *Remote Sens.*, vol. 13, no. 16, Aug. 2021, Art. no. 3204, doi: 10.3390/rs13163204.

[11] C. Y. Zhao, Z. Lu, Q. Zhang, C. S. Yang, and W. Zhu, "Mining collapse monitoring with SAR imagery data: A case study of datong mine, China," *J. Appl. Remote Sens.*, vol. 8, Aug. 2014, Art. no. 3574, doi: 10.1117/1.JRS.8.083574.

[12] S. Y. Wang et al., "Evaluating the feasibility of illegal open-pit mining identification using InSAR coherence," *Remote Sens.*, vol. 12, no. 3, Feb. 2020, Art. no. 367, doi: 10.3390/rs12030367.

[13] P. Lu, N. Casagli, F. Catani, and V. Tofani, "Persistent scatterers interferometry hotspot and cluster analysis (PSI-HCA) for detection of extremely slow-moving landslides," *Int. J. Remote Sens.*, vol. 33, no. 2, pp. 466–489, Mar. 2012, doi: 10.1080/01431161.2010.536185.

[14] P. Lu, S. B. Bai, V. Tofani, and N. Casagli, "Landslides detection through optimized hot spot analysis on persistent scatterers and distributed scatterers," *ISPRS J. Photogramm.*, vol. 156, pp. 147–159, Oct. 2019, doi: 10.1016/j.isprsjprs.2019.08.004.

[15] K. X. Zhu, P. H. Xu, C. Cao, L. J. Zheng, Y. Liu, and X. J. Dong, "Preliminary identification of geological hazards from Songpinggou to Feihong in Mao County along the Minjiang River using SBAS-InSAR technique integrated multiple spatial analysis methods," *Sustainability*, vol. 13, no. 3, Feb. 2021, Art. no. 1017, doi: 10.3390/su13031017.

[16] H. Y. Dai et al., "Landslide identification and gradation method based on statistical analysis and spatial cluster analysis," *Remote Sens.*, vol. 14, no. 18, Sep. 2022, Art. no. 4504, doi: 10.3390/rs14184504.

[17] Z. R. Wu, P. F. Ma, Y. Zheng, F. Gu, L. Liu, and H. Lin, "Automatic detection and classification of land subsidence in deltaic metropolitan areas using distributed scatterer InSAR and oriented R-CNN," *Remote Sens. Environ.*, vol. 290, May 2023, Art. no. 3545, doi: 10.1016/j.rse.2023.113545.

[18] C. Jiang, L. Wang, X. X. Yu, S. S. Chi, T. Wei, and X. L. Wang, "DPIM-Based InSAR phase unwrapping model and a 3D mining-induced surface deformation extracting method a case of Huainan mining area," *KSCE J. Civil Eng.*, vol. 25, no. 2, pp. 654–668, Dec. 2021, doi: 10.1007/s12205-020-5288-0.

[19] C. Jiang, L. Wang, and X. X. Yu, "Retrieving 3D large gradient deformation induced to mining subsidence based on fusion of Boltzmann prediction model and single-track InSAR Earth observation technology," *IEEE Access*, vol. 9, pp. 87156–87172, 2021, doi: 10.1109/ACCESS.2021.3089160.

[20] X. P. Diao, K. Wu, D. H. Hu, L. Li, and D. W. Zhou, "Combining differential SAR interferometry and the probability integral method for three-dimensional deformation monitoring of mining areas," *Int. J. Remote Sens.*, vol. 37, no. 21, pp. 5196–5212, Nov. 2016, doi: 10.1080/01431161.2016.1230284.

[21] Y. Chen, Y. X. Tong, and K. Tan, "Coal mining deformation monitoring using SBAS-InSAR and offset tracking: A case study of Yu County, China," *IEEE J. Sel. Topics Appl. Earth Observ. Remote Sens.*, vol. 13, pp. 6077–6087, 2020, doi: 10.1109/JSTARS.2020.3028083.

[22] J. Q. Ma, J. C. Yang, Z. R. Zhu, H. S. Cao, S. B. Li, and X. L. Du, "Decision-making fusion of InSAR technology and offset tracking to study the deformation of large gradients in mining areas-Xuemiaotan mine as an example," *Front. Earth Sci.*, vol. 10, Aug. 2022, Art. no. 962362, doi: 10.3389/feart.2022.962362.

[23] S. Q. Wang, Z. C. Bai, Y. P. Lv, and W. Zhou, "Monitoring extractive activity-induced surface subsidence in highland and alpine opencast coal mining areas with multi-source data," *Remote Sens.*, vol. 14, no. 14, Jul. 2022, Art. no. 3442, doi: 10.3390/rs14143442.

[24] H. Tan, X. X. Yu, M. F. Zhu, Z. C. Guo, and H. Z. Chen, "Deformation monitoring and spatiotemporal evolution of mining area with unmanned aerial vehicle and D-InSAR technology," *Mobile Inf. Syst.*, vol. 2022, May 2022, Art. no. 8075611, doi: 10.1155/2022/8075611.

[25] S. L. Furst, S. Doucet, P. Vernant, C. Champollion, and J. L. Carme, "Monitoring surface deformation of deep salt mining in Vauvert (France), combining InSAR and leveling data for multi-source inversion," *Solid Earth.*, vol. 12, no. 1, pp. 15–34, Jan. 2021, doi: 10.5194/se-12-15-2021.

[26] M. Wei, D. Sandwell, and B. Smith-Konter, "Optimal combination of InSAR and GPS for measuring interseismic crustal deformation," *Adv. Space Res.*, vol. 46, no. 2, pp. 236–249, Jul. 2010, doi: 10.1016/j.asr.2010.03.013.

[27] B. Q. Chen, K. H. Deng, H. D. Fan, and H. Ming, "Large-scale deformation monitoring in mining area by D-InSAR and 3D laser scanning technology integration," *Int. J. Mining Sci. Technol.*, vol. 23, no. 4, pp. 555–561, Jul. 2013, doi: 10.1016/j.ijmst.2013.07.014.

[28] V. B. Prush and R. B. Lohman, "Time-varying elevation change at the centralia coal mine in Centralia, Washington (USA), constrained with InSAR, ASTER, and optical imagery," *IEEE J. Sel. Topics Appl. Earth Observ. Remote Sens.*, vol. 8, no. 2, pp. 919–925, Feb. 2015, doi: 10.1109/JSTARS.2014.2348412.

[29] Z. F. Yang et al., "An extension of the InSAR-Based probability integral method and its application for predicting 3-D mining-induced displacements under different extraction conditions," *IEEE Trans. Geosci. Remote Sens.*, vol. 55, no. 7, pp. 3835–3845, Jul. 2017, doi: 10.1109/TGRS.2017.2682192.

[30] J. Chuang, W. Lei, X. Y. Yu, S. S. Chi, W. Tao, and Z. C. Guo, "A DPIM-InSAR method for monitoring mining subsidence based on deformation information of the working face after mining has ended," *Int. J. Remote Sens.*, vol. 42, no. 16, pp. 6333–6361, Aug. 2021, doi: 10.1080/01431161.2021.1931540.

[31] Z. J. Liu et al., "Efficient identification and monitoring of landslides by time-series InSAR combining single- and multi-look phases," *Remote Sens.*, vol. 14, no. 4, Feb. 2022, Art. no. 1026, doi: 10.3390/rs14041026.

[32] Y. S. Li, J. F. Zhang, Z. H. Li, Y. Luo, W. L. Jiang, and Y. F. Tian, "Measurement of subsidence in the Yangbajing geothermal fields, Tibet, from TerraSAR-X InSAR time series analysis," *Int. J. Digit. Earth*, vol. 9, no. 7, pp. 697–709, Nov. 2016, doi: 10.1080/17538947.2015.1116624.

[33] D. P. S. Bekaert, A. Hooper, and T. J. Wright, "A spatially variable power law tropospheric correction technique for InSAR data," *J. Geophys. Res.: Solid Earth.*, vol. 120, no. 2, pp. 1345–1356, Feb. 2015, doi: 10.1002/2014JB011558.

[34] L. K. Dong et al., "Time series InSAR three-dimensional displacement inversion model of coal mining areas based on symmetrical features of mining subsidence," *Remote Sens.*, vol. 14, no. 4, Feb. 2022, Art. no. 2143, doi: 10.3390/rs13112143.

[35] T. H. Grubesic, R. Wei, and A. T. Murray, "Spatial clustering overview and comparison: Accuracy, sensitivity, and computational expense," *Ann. Assoc. Amer. Geographers*, vol. 104, no. 6, pp. 1134–1156, Nov. 2014, doi: 10.1080/00045608.2014.958389.

[36] Y. Ma and X. Zhao, "*POD*: A parallel outlier detection algorithm using weighted kNN," *IEEE Access*, vol. 9, pp. 286–306, 2021, doi: 10.1109/ACCESS.2021.3085605.

[37] P. Zhang, Z. H. Guo, S. F. Guo, and J. Xia, "Land subsidence monitoring method in regions of variable radar lection characteristics by integrating PS-InSAR and SBAS-InSAR techniques," *Remote Sens.*, vol. 14, no. 14, Jul. 2022, Art. no. 3265, doi: 10.3390/rs14143265.

[38] A. Y. Alfakih, "On the uniqueness of Euclidean distance matrix completions," *Linear Algebra Appl.*, vol. 269, pp. 1–14, Sep. 2003, doi: 10.1016/S0024-3795(02)00737-1.

[39] Y. W. Chen et al., "KNN-BLOCK DBSCAN: Fast clustering for large-scale data," *IEEE Trans. Syst., Man, Cybern.: Syst.*, vol. 51, no. 6, pp. 3939–3953, Jun. 2021, doi: 10.1109/TSMC.2019.2956527.

[40] D. Q. Ge, L. Zhang, Y. Wang, X. F. Guo, and Y. Xia, "Merging multi-track PSI result for land subsidence mapping over very extended area," in *Proc. IEEE Int. Geosci. Remote Sens. Symp.*, 2010, pp. 3522–3525, doi: 10.1109/IGARSS.2010.5652430.

[41] B. Schaffrin and A. Wieser, "On weighted total least-squares adjustment for linear regression," *J. Geodesy*, vol. 82, no. 7, pp. 415–421, May 2020, doi: 10.1007/s00190-007-0190-9.

[42] J. Hu, Z. W. Li, X. L. Ding, J. J. Zhu, L. Zhang, and Q. Sun, "Resolving three-dimensional surface displacements from InSAR measurements: A review," *Earth-Sci. Rev.*, vol. 133, pp. 1–17, Jun. 2014, doi: 10.1016/j.earscirev.2014.02.005.

[43] Y. F. Sun et al., "Influence of coal mining on historical buildings: Case Study in Shanxi," *Int. J. Environ. Res. Public Health*, vol. 20, no. 2, Jan. 2023, Art. no. 1543, doi: 10.3390/ijerph20021543.

[44] R. L. Miao et al., "Characteristics of fluvial sedimentary reservoir configuration of middle permian Shihezi formation in Wuxiang area," *J. Minerals Petrol.*, vol. 40, no. 4, pp. 97–104, Apr. 2020, doi: 10.19719/j.cnki.1001-6872.2020.04.10.

[45] H. Karabork, H. B. Makineci, O. Orhan, and P. Karakus, "Accuracy assessment of DEMs derived from multiple SAR data using the InSAR technique," *Arabian J. Sci. Eng.*, vol. 46, no. 6, pp. 5755–5765, Jun. 2021, doi: 10.1007/s13369-020-05128-8.

[46] H. Y. Jia, Y. J. Wang, D. Q. Ge, Y. K. Deng, and R. Wang, "InSAR study of landslides: Early detection, Three-dimensional, and long-term surface displacement estimation–A case of Xiaojiang River Basin, China," *Remote Sens.*, vol. 14, no. 7, pp. 1759, Apr. 2022, doi: 10.3390/rs14071759.

[47] Y. Kang, Z. Lu, C. Y. Zhao, Y. K. Xu, J. W. Kin, and A. J. Gallegos, "InSAR monitoring of creeping landslides in mountainous regions: A case study in Eldorado National Forest, California," *Remote Sens. Environ.*, vol. 258, Jun. 2021, Art. no. 112400, doi: 10.1016/j.rse.2021.112400.

[48] K. Yuvaraj and U. S. Ragupathy, "Hybrid active contour mammographic mass segmentation and classification," *Comput. Syst. Sci. Eng.*, vol. 40, no. 3, pp. 823–834, May 2022, doi: 10.32604/csse.2022.018837.

[49] H. C. Zhu, W. Huang, and H. Y. Liu, "Loess terrain segmentation from digital elevation models based on the region growth method," *Phys. Geogr.*, vol. 39, no. 1, pp. 51–66, Jun. 2018, doi: 10.1080/02723646.2017.1342215.

[50] Z. Y. Wang et al., "Analyzing, and modeling for single subsidence basin in coal mining areas based on SAR interferometry with L-band data," *Sci. Program.*, vol. 2021, no. 6, pp. 1–10, Feb. 2021, doi: 10.1155/2021/6662097.

Lu Li was born in Shaanxi, China, in 1996. He received the M.S. degree in surveying and mapping in 2020 from China University of Geosciences, Beijing, China, where he is currently working toward the Ph.D. degree in communication and information systems with the Department of Space Microwave Remote Sensing System, Aerospace Information Research Institute, Chinese Academy of Sciences, Beijing, China.

He is also with the University of Chinese Academy of Sciences, Beijing. His research interests include mining subsidence and disaster monitoring using SAR technology.

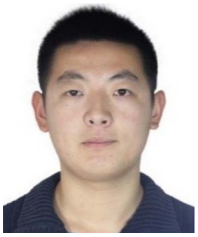

Jili Wang (Member, IEEE) received the B.S. degree in information warfare technology from the Beijing Institute of Technology, Beijing, China, in 2013, and the Ph.D. degree in communication and information systems from the University of Chinese Academy of Sciences, Beijing, in 2019.

From 2016 to 2017, he was a Research Assistant with the Institute of Space and Earth Information Science, The Chinese University of Hong Kong, Hong Kong. Since 2019, he has been with the Spaceborne Microwave Remote Sensing System Department, Aerospace Information Research Institute, Chinese Academy of Sciences, Beijing. His research interests include the development of SAR Interferometry techniques, time-series InSAR processing techniques, and their applications on DEM generation and deformation parameter estimation.

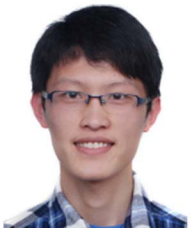

Heng Zhang (Member, IEEE) received the B.S. degree in electronic information science from Nanjing University, Nanjing, China, in 2013, and the Ph.D. degree in communication and information systems from the University of Chinese Academy of Sciences, Beijing, China, in 2018.

In 2018, he joined the Aerospace InformationResearch Institute, Chinese Academy of Sciences, Beijing. His research interests include bistaticsynthetic aperture radar imaging and interferometry.

Yi Zhang received the M.S. and Ph.D. degrees in communication and information system from the Graduate University of Chinese Academy of Sciences, Beijing, China, in 2002 and 2012, respectively.

He is currently a Researcher and the Director of the Project Office with the Institute of Electronics, Chinese Academy of Sciences, Beijing. His research interests include SAR system design and related signal processing, involving SAR image processing and applications and digital signal processing hardware design.

Yingjie Wang received the B.S. degree in communication engineering from the Beijing Institute of Technology, Beijing, China, in 2013, and the Ph.D. degree in communication and information systems from the Institute of Electronics, Chinese Academy of Sciences, Beijing, in 2018.

In 2018, she was with the Aerospace Information Research Institute, Chinese Academy of Sciences (AIR-CAS), where she worked on spaceborne interferometric synthetic aperture radar (InSAR) technology. Her main research interests include InSAR techniques, particularly focused on multitemporal InSAR and their applications on natural hazards and urban monitoring, and 3-D deformation monitoring technology.

Yuanzhao Fu was born in Shaanxi, China, in 1999. He received the B.S. degree in surveying and mapping engineering from China University of Mining and Technology, Xuzhou, China, in 2021. He is currently working toward the Ph.D. degree in communication and information systems with the Department of Space Microwave Remote Sensing System Department, Aerospace Information Research Institute, Chinese Academy of Sciences, Beijing, China.

He is also with the University of Chinese Academy of Sciences, Beijing. His research interests include multisource data fusion and time series InSAR.